Electronic materials

Influence of strain and external electric field on the performance of PC$_6$/MoSe$_2$ heterostructure

Shuang Han[1], Xiumei Wei[1,*] , Yuhong Huang[1], Jianming Zhang[1], Gangqiang Zhu[1], and Jian Yang[1]

[1] School of Physics & Information Technology, Shaanxi Normal University, Xi'an 710119, Shaanxi, China

ABSTRACT

In this work, the structural, electronic and optical performances of PC$_6$/MoSe$_2$ heterostructure are investigated using first principles calculations based on density functional theory. The PC$_6$/MoSe$_2$ heterostructure displays type-I band alignment with a direct band gap of 0.84 eV, and its CBM and VBM are contributed by PC$_6$. The heterojunction can be transformed from type-I to type-II under biaxial strain, even from semiconductor to metal in the presence of a strong strain within the range of elastic response. Meanwhile, the transition from type-I to type-II can be also observed when an electric field greater than 0.3 V/Å is applied. So the electronic properties of the PC$_6$/MoSe$_2$ heterostructure can be effectively modulated by applying biaxial strain and external electric field, which provides great potential for designing multifunctional devices. In addition, the optical absorption spectrum reveals that the PC$_6$/MoSe$_2$ heterostructure could present a good optical utilization performance, indicating that it may play an important role in the application of optoelectronic devices. The results suggest that the PC$_6$/MoSe$_2$ heterostructure can be widely used in optoelectronic, photocatalytic and light-emitting applications in future research.

Introduction

Two-dimensional (2D) materials have attracted great attention due to their unique characteristics, such as high carrier mobility, excellent mechanical properties and optical properties [1–3]. Transition metal 2D materials include transition metal dichalcogenides (TMDs), transition metal carbides (TMCs), transition metal oxides (TMOs) and so on. Among them, the most studied are TMDs, which have intriguing electronic, optical and thermal properties [4, 5], such as MoS$_2$ [6–9], MoSe$_2$ [10–13] and WSe$_2$ [14–16]. However, the carrier mobility of TMDs is low, which limits their practical applications [17]. Several studies reveal that the performance of single materials can be optimized by constructing heterostructures [18–21]. The heterostructure can not only maintain the

⁂ Springer

intrinsic characteristics of the single-layer material, but also obtain new electronic properties due to the interface coupling effect of the heterostructure at the interface. As a 2D transition metal dichalcogenide, $MoSe_2$ has high absorption efficiency and is often used to construct heterostructures due to its unique lattice structure, electron transport and optical properties. For example, $MoSe_2$@rGO cathode-coated batteries provide a higher reversible capacity and excellent cycle stability [22]. Tian et al. found that the photocatalytic activity of $ZnSe/MoSe_2$ is four times that of ZnSe, and its photoelectric performance is also increased [23].

PC_6 is a layered semiconductor material with a graphene-like structure [24], which has attracted the attention of researchers due to its extremely high intrinsic conductivity with anisotropy character and ultrahigh carrier mobility [25]. For example, it has very good application performance in the field of Li-ion batteries [26] and could be a potential reusable material as NO and NO_2 sensors with high selectivity and sensitivity [27]. Unfortunately, PC_6 has a lower optical absorption efficiency [24], which limits its application in optoelectronics. Therefore, we can improve its optical absorption efficiency by constructing heterostructures with $MoSe_2$. It is well-known that the band alignment of heterojunction can be tuned by electric field and strain. For example, $InSe/MoSe_2$ (WSe_2) [28] and $g-C_3N_4/WSe_2$ [29] exhibit a variety of band alignments under different external electric fields, including astraddle type-I, interlaced type-II and broken-up type-III. When biaxial strain is applied, the $GaS/g-C_3N_4$ can transition from type-I to type-II band alignment, even from semiconductor to metal under strong strain [30]. Similarly, the band edge of the blue phosphorene/C_2N heterostructure can be tuned by applying biaxial strain [31]. In addition, vacancies usually play an important role in tailoring electronic, optical, and magnetic properties of semiconductors. For $MoSe_2$, whether it is Mo-vacancy [32] or Se-vacancy [33], it should be beneficial to their potential applications in optoelectronics and nanoelectronic devices. However, the influence of different biaxial strains and electric fields on the $PC_6/MoSe_2$ heterostructure is the important points of our work.

In this paper, we establish $PC_6/MoSe_2$ heterostructure, and the structure, electronic and optical properties of the $PC_6/MoSe_2$ heterostructure are investigated using density functional theory. It

turns out that the $PC_6/MoSe_2$ heterostructure exhibits a type-I band alignment. Type-I band alignment is very useful for confining electrons and holes in the same material, so type-I heterostructures are mainly used in light-emitting diodes and semiconductor lasers. The transition from type-I to type-II is completed under external electric field and strain, even from semiconductor to metal under strong strain, which provides guidance for extending the application of $PC_6/MoSe_2$ heterostructure.

Computational method

All the first-principles calculations are performed using Vienna Ab initio Simulation Package (VASP) [34, 35], and based on periodic density functional theory (DFT) [36, 37] and projector augmented wave (PAW) [38, 39] method. Since the Perdew–Burke–Ernzerhof (PBE) [40, 41] method of generalized gradient approximation usually underestimates the band gap of semiconductors, we use Heyd–Scuseria–Ernzerhof (HSE06) [42] hybrid functional to describe the electronic and optical properties of $PC_6/MoSe_2$ heterostructure. The optB88-vdW functional is selected to describe the vdW interaction in the heterojunction. The cut-off energy for the plane wave is set to 400 eV. All structures are fully relaxed, and convergence criterion of energy in the self-consistency process is set to 10^{-4} eV. The interaction between adjacent periodic slabs can be avoided when the vacuum layer is set to 20 Å. A Monkhorst–Pack k-point mesh of $3 \times 3 \times 1$ is adopted to optimize the geometric structures and perform the self-consistent calculations. It is well-known that PBE usually underestimates the band gap. Therefore, we adopt the HSE functional in the following calculations. An external electric field [43, 44] is implemented by introducing a planar dipole layer, which will cause a uniform potential difference along the direction perpendicular to the heterojunction interface.

Results and discussion

Geometry and electronic structure of monolayers

The optimized crystal structures of PC_6 and $MoSe_2$ monolayers are shown in Fig. 1 with the lattice

constants 6.683 Å and 3.327 Å, respectively, which are consistent with previous theoretical reports [27, 29]. The thickness of the PC_6 monolayer is about 2.140 Å, because the P atoms in the graphene-like PC_6 are extruded to both sides. The bond lengths in PC_6 are 1.811 Å for P–C, 1.361 Å for C1-C2, 1.462 Å for C2-C3 and C4-C5 and 1.422 Å for C3-C4, while the bond length of Mo-Se is 2.547 Å in $MoSe_2$, which are in good agreement with the literatures [24, 45].

The band structures calculated by HSE06 are shown in Fig. 2. It is shown that both PC_6 and $MoSe_2$ are direct semiconductors, and their conduction band minimum (CBM) and valence band maximum (VBM) are located at the M point and K point with the band gaps of 0.94 eV and 1.8 eV, respectively, which is in accordance with the previous study [23, 25].

Geometric and electronic structure of the PC_6/$MoSe_2$ heterostructure

As mentioned above, the optimized lattice constants for the PC_6 and $MoSe_2$ monolayers are 6.67 Å and 3.33 Å, respectively. Therefore, to construct the PC_6/$MoSe_2$ heterostructure, a $2 \times 2 \times 1$ $MoSe_2$ supercell is used to match the $1 \times 1 \times 1$ PC_6 unit cell, as shown in Fig. 3. In this way, the lattice constant of the heterostructure is $a = 6.67$ Å with the lattice mismatch of only about 0.1%. Then, after geometrical relaxation, the P–C, C–C and Mo-Se bond lengths at the interface change slightly, which implies that there is little rearrangement of atoms. In order to obtain a relatively stable structure, the binding energy (E_b) of the PC_6/$MoSe_2$ heterostructure is calculated, which is defined as follows:

$$E_b = E_{PC_6/MoSe_2} - E_{PC_6} - E_{MoSe_2} \qquad (1)$$

here, $E_{PC_6/MoSe_2}$ is the total energy of the PC_6/$MoSe_2$ heterostructure, while E_{PC_6} and E_{MoSe_2} are the total energies of the isolated PC_6 and $MoSe_2$ monolayers, respectively. According to Eq. (1), the binding energy of the relaxed PC_6/$MoSe_2$ heterostructure is -0.496 meV. It is well-known that a negative value of the binding energy means that the formation of the heterostructure is an exothermic process, which proves the stability of the heterostructure.

The band structure in Fig. 4a indicates that the PC_6/$MoSe_2$ heterostructure is a semiconductor with a direct band gap of 0.88 eV, which is smaller than the band gap of single-layer PC_6 (0.94 eV) and $MoSe_2$ (1.85 eV), indicating the weak charge transfer between PC_6 and $MoSe_2$ monolayers. For further identifying the electronic properties of the PC_6/$MoSe_2$ heterostructure, the density of state (DOS) is calculated, as shown in Fig. 4b. The weak hybridization between PC_6 and $MoSe_2$ can be found, indicating that the interlayer coupling between the two layers is weak. It can be said that the intrinsic electronic properties are preserved when PC_6 monolayer transforms into PC_6/$MoSe_2$ heterostructure. The DOS of PC_6/$MoSe_2$ heterostructure shows that the CBM and VBM are contributed by C-2p, so electrons and holes are confined in PC_6, which means that a type-I heterostructure is formed. This type of heterostructure can be used in optoelectronic devices, such as light-emitting diodes.

Work function is an important factor in determining the charge transfer between layers and then may affect the band alignment of heterostructures. The work functions are 4.928 eV and 5.575 eV for the PC_6 and $MoSe_2$ monolayers, respectively. The difference between the work functions will cause electrons to flow from PC_6 to $MoSe_2$. Hence, the electrons accumulate near $MoSe_2$, while the holes accumulate in the region of PC_6, thereby forming a built-in electric field directed from PC_6 to $MoSe_2$, which may produce an extra driving force. To more clearly describe the

Figure 1 Crystal structure of single layer **a** PC_6 and **b** $MoSe_2$. Brown, purple, pink and dark green represent C, P, Se and Mo, respectively.
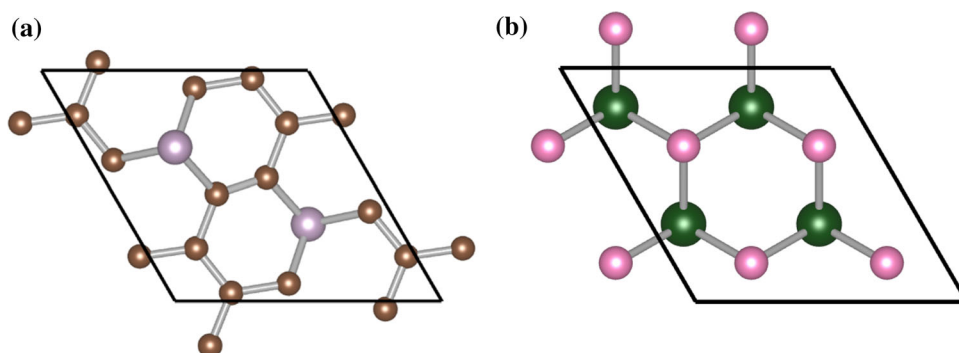
(a)

(b)

Figure 2 Band structures of **a** monolayer PC_6 and **b** monolayer $MoSe_2$ through HSE06. The Fermi level is set to zero and indicated by the dashed line.
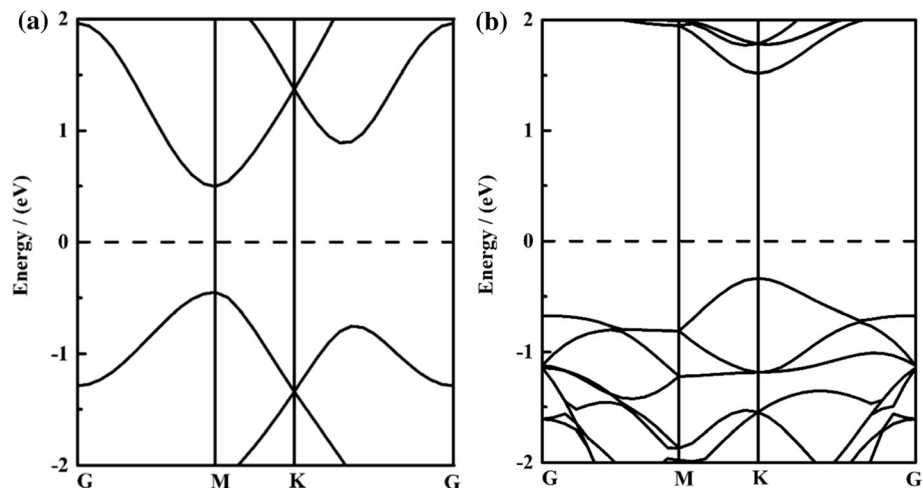
Figure 3 a Side view and **b** top view of the geometry of the $PC_6/MoSe_2$ heterostructure. Brown, purple, pink and dark green represent C, P, Se and Mo, respectively.
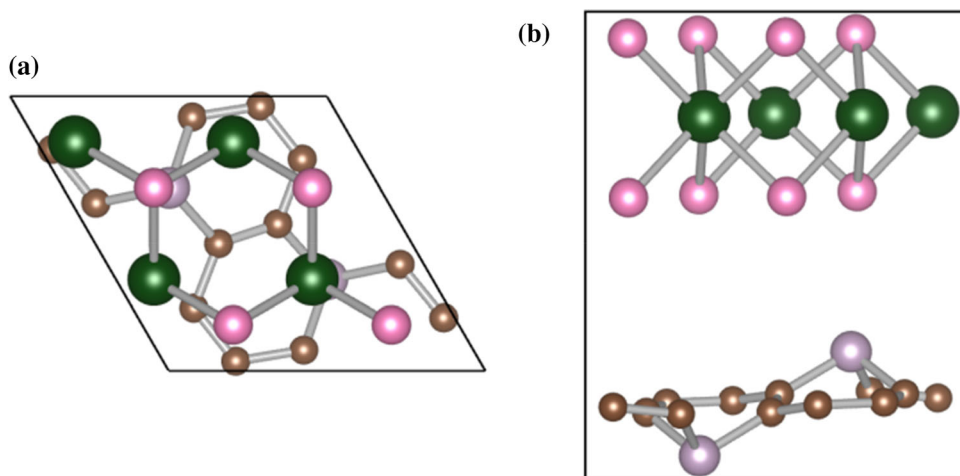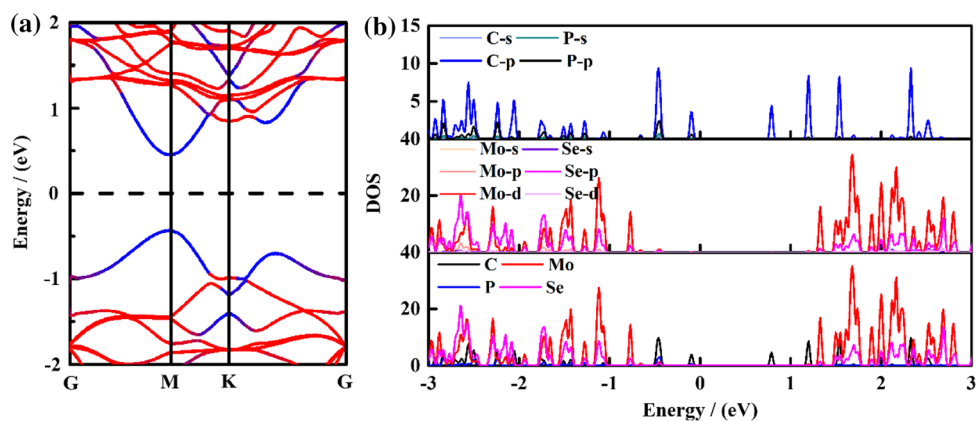
Figure 4 a Band structure and **b** DOS of $PC_6/MoSe_2$ heterostructure. In the band structure, blue and red lines represent the contributions of PC_6 and $MoSe_2$ layers, respectively. The Fermi level is set to zero and indicated by the dashed line.

interfacial coupling between PC_6 and $MoSe_2$, the charge density difference of the $PC_6/MoSe_2$ heterostructure is calculated as:

$$\Delta\rho = \rho_{PC_6/MoSe_2} - \rho_{PC_6} - \rho_{MoSe_2} \qquad (2)$$

where $\rho_{PC_6/MoSe_2}$, ρ_{PC_6} and ρ_{MoSe_2} are the charge density of $PC_6/MoSe_2$ heterostructure, single-layer PC_6 and $MoSe_2$, respectively. The charge density rearrangement can be found in both layers and the charge transfer between them can be realized, as shown in

Fig. 5a. An obvious planar charge rearrangement and the transfer of electrons from PC_6 to $MoSe_2$ are observed except the vicinity of the P atoms, where the buckling exists. To further explore the properties of charge transfer, the averaged charge density difference is calculated and shown in Fig. 5b, in which the positive values indicate electron accumulation, and the negative values represent electron depletion. At the interface, the charge transfer is complicated, which is also resulted from the buckling in the structure, although a small transfer of electron from PC_6 to $MoSe_2$ can be deduced from the figure. Then, the Bader charge analysis is performed to quantitatively confirm the total value of the transferred charge, which shows that the transferred electron is 0.0173e from PC_6 to $MoSe_2$.

Effect of strain on the PC_6/$MoSe_2$ heterostructure

The electronic structural properties of heterostructures can be adjusted under biaxial strains, which have been widely used in 2D materials [46, 47]. Applying biaxial strain can improve the performance of materials, which is important for further applications [48, 49]. Therefore, the effect of biaxial strain on the performance of heterojunction is investigated. The biaxial strain of PC_6/$MoSe_2$ heterostructure can be defined as:

$$\delta = \left(\frac{a - a_0}{a_0} \right) \times 100\% \tag{3}$$

where a and a_0 represent the strained and unstrained lattice constants. So as to ensure that the applied strain is within the elastic limit, the strain energy (E_s) of each atom in the system is calculated,

$$E_s = (E_{strained} - E_{unstrained})/n \tag{4}$$

where n is the total number of atoms in the unit. Figure 6a shows that the strain energy approximatively presents a quadratic curve in the selected range of ± 6%, which indicates that the geometry of the heterostructure is not destroyed under the biaxial strain, that is, the applied biaxial strain is reasonable and the process is completely reversible. The band gap of the heterostructure is also plotted as a function of strain in Fig. 6a. It can be seen that the band gap decreases almost linearly as the strain increases within the range of -6% ~ 5%, and it reaches the maximum value (~ 1.29 eV) under the strain of about -5%. At $\delta = 6\%$, the system undergoes a direct transition of semiconductor to metal, which means that the conductivity of the heterostructure is adjustable. Then, we focused on semiconductor and supply the band edges under the strain of -6% to 5% in Fig. 6b. Apparently, type-I band alignment is maintained from -5% to 5% strain. It is noticed that the band gaps of both the two single layers decrease from negative to positive strain by and large except in the range of great compression for $MoSe_2$, where the band gap of PC_6 is more sensitive to strain. At the
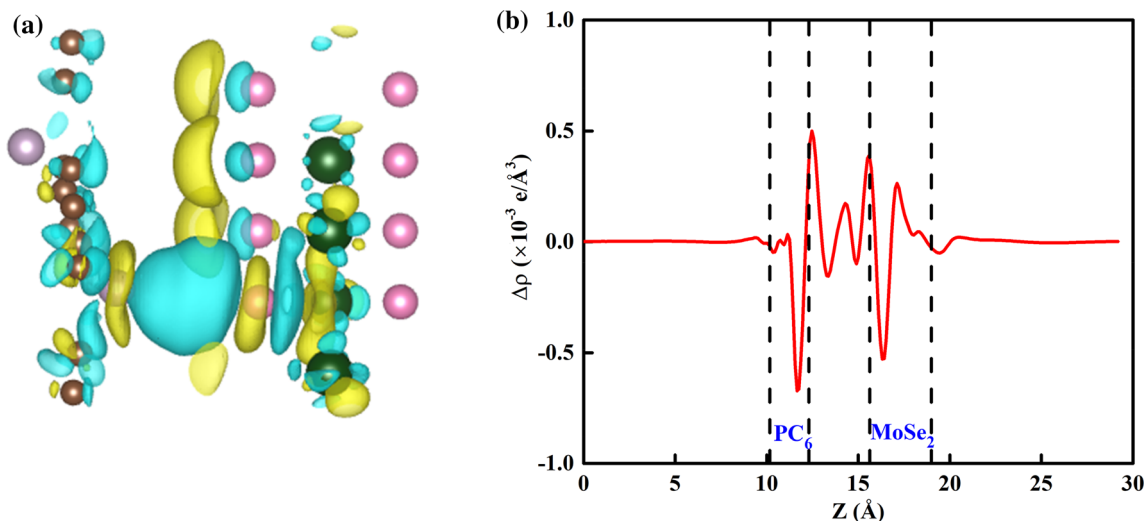

Figure 5 **a** Charge density difference for the PC_6/$MoSe_2$ heterostructure, the cyan and yellow regions represent the charge depletion and accumulation, respectively. **b** The averaged charge density difference for the PC_6/$MoSe_2$ heterostructure along the Z-axis.
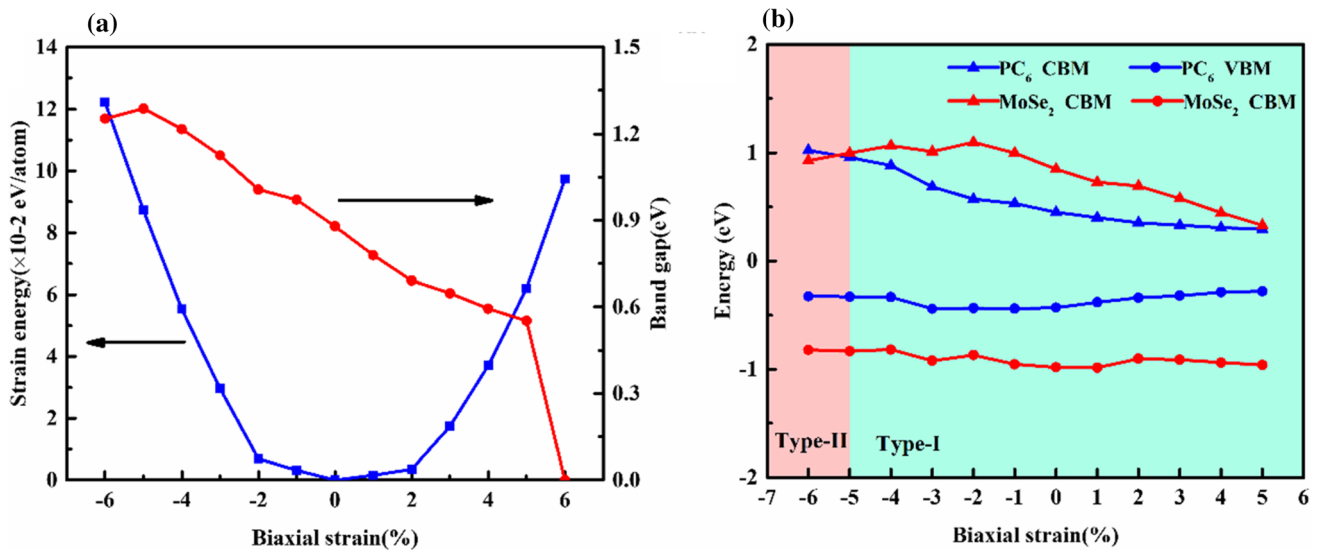
Figure 6 a In-plane biaxial strain effects on the band gap and strain energy of the $PC_6/MoSe_2$ heterostructure. **b** VBM and CBM levels of $PC_6/MoSe_2$ heterostructure under different applied biaxial strains. A positive value of strain indicates stretching strain. Fermi level is set to 0.

meantime, it also can be seen that for both materials, the VBM hardly changes with strains, and the change of gap is basically determined by CBM. The CBM of PC_6 decreases monotonically as the strain increases from negative to positive, while the CBM of $MoSe_2$ increases monotonously from -6% to -4%, leading to a transition from type-I to type-II between -6% and -5%. In short, the strain can effectively change the type of $PC_6/MoSe_2$ heterostructure. It is useful for designing multifunctional electronic and optoelectronic devices.

Figure 7 shows the effect of different strains on DOS. The DOS of the conduction band shifts slightly to lower energy as the positive strain increases. With the increase in negative strain, the DOS of the conduction band obviously shifts to higher energy. It is obvious for the movement of occupation by C atoms, but the movement of occupation by Mo atom is not obvious, so that Mo atoms dominate the CBM at -6%. Therefore, the band gap increase almost linearly as the strain decreases within the range of 5% ~ -6%, and it reaches the maximum value under the strain of about -5%. When $PC_6/MoSe_2$ remains type-I heterojunction, the main electronic state (C atoms) occupied at the edge of the band gap is almost the same as the case without strain in Fig. 4b. Obviously, the occupancy rate of C atoms in CBM and VBM becomes larger from positive to negative strain. As shown in Fig. 4b, the occupancy of electrons is relatively

dispersed, indicating that the localization of electrons is weakened. However, strain can change the occupation of electrons, especially at -1.2 ~ -1.5 eV and 1.2 ~ 2 eV, and the sharp peaks of Mo atoms in DOS increase and the occupation of electrons gradually converges as the positive strain increases, indicating that the electrons are relatively localized. The peak value of DOS gradually decreases as the negative strain increases, especially for Se atoms.

The effect of vertical strain on the band gap of the $PC_6/MoSe_2$ heterostructure is shown in Table 1. The vertical strain is defined as: $\varepsilon = d - d_0$, where $d_0 = 3.7$ Å is the original distance between the two layers. It is shown that the vertical strain has little effect on the band structure of the $PC_6/MoSe_2$ heterostructure, so no much work is done on it.

Effect of external electric field on the $PC_6/MoSe_2$ heterostructure

To explore the effect of external electric field on the electronic properties of the $PC_6/MoSe_2$ heterostructure, the external electric field in the range of -0.5 to 0.5 V/Å is applied on the heterostructure with the positive direction perpendicularly from $MoSe_2$ to PC_6. Figure 8 shows the variation of band edges and band gaps of PC_6 and $MoSe_2$ in the $PC_6/MoSe_2$ heterostructure under various external electric fields. It can be seen that both the VBM and CBM of $MoSe_2$ decrease monotonically from positive electric field to
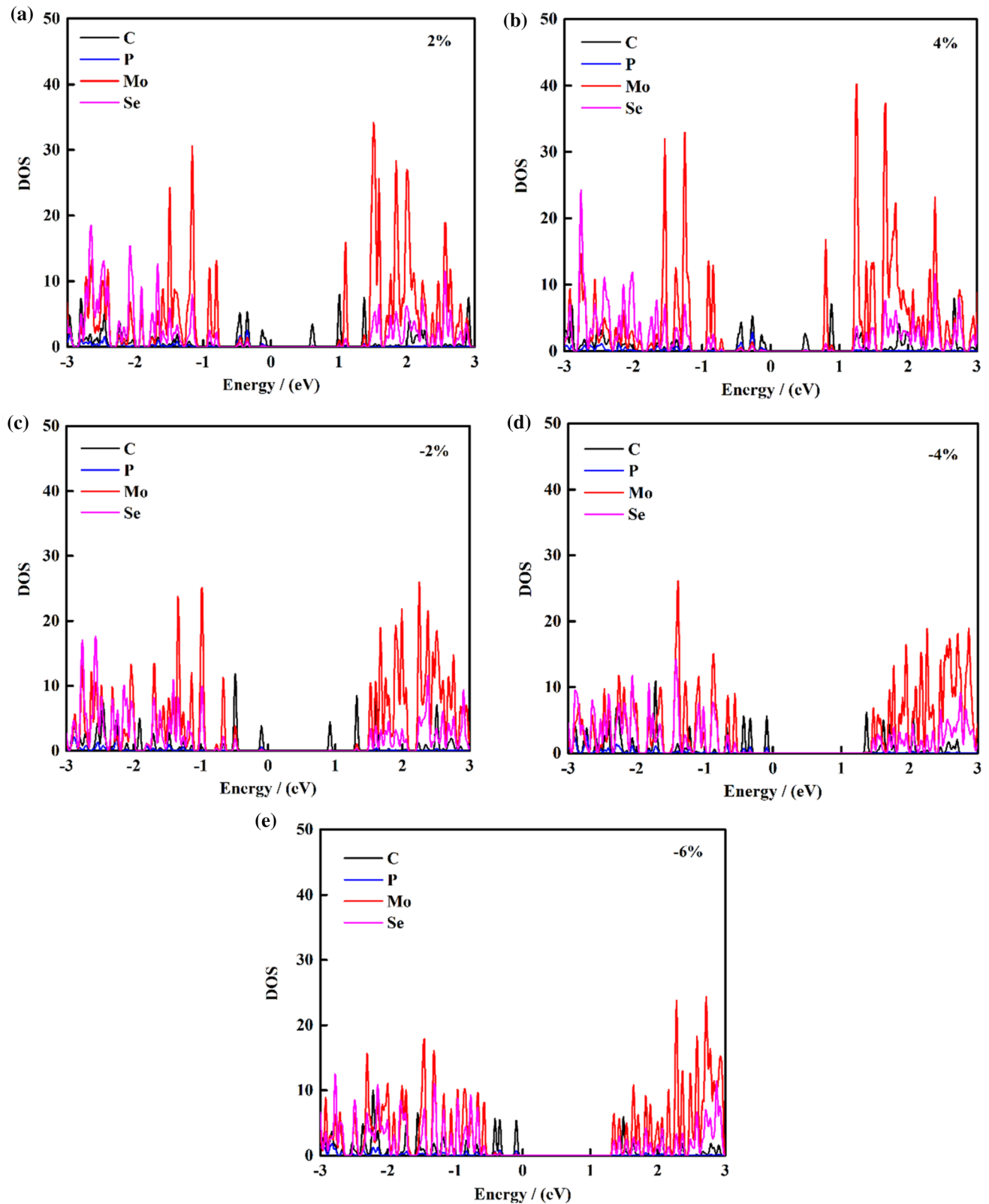
Figure 7 DOS of $PC_6/MoSe_2$ heterostructure at strains of **a** 2%, **b** 4%, **c** -2%, **d** -4% and **e** -6%. Please refer to the electronic version.

Table 1 Band gap of PC$_6$/MoSe$_2$ heterostructure under different applied vertical strains

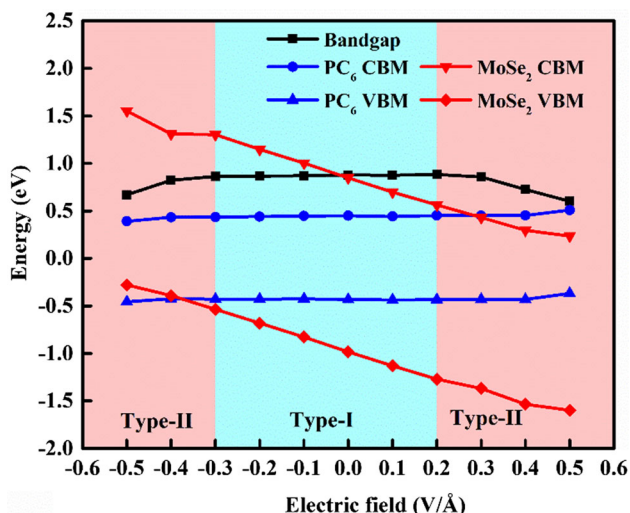| ε(Å)	0.8	0.6	0.4	0.2	0	-0.2	-0.4	-0.6	-0.8
E$_g$(eV)	0.890	0.864	0.882	0.859	0.879	0.869	0.870	0.879	0.841

Figure 8 Calculated band gap and band edge position as a function of the vertical electric field for the PC$_6$/MoSe$_2$ heterostructure.

negative electric field (due to potential difference of the external electric field), while that of PC$_6$ change little especially in the range of -0.4 ~ 0.4 V/Å. So the MoSe$_2$ layer is more sensitive to external electric field on the heterostructure. The CBM and VBM of the heterojunction are contributed by PC$_6$ monolayer from -0.3 to 0.2 V/Å, resulting in the band gap of the heterojunction remaining almost unchanged in the range. When a positive electric field is strengthened, the CBM of MoSe$_2$ gradually approaches the Fermi level (the Fermi level rises). Once the negative electric field exceeds 0.3 V/Å, the CBM of the heterostructure is contributed by MoSe$_2$, and the VBM is still contributed by PC$_6$. Finally, the transition from type-I to type-II is completed, and the spatial distribution of carriers has changed. On the other hand, when a negative electric field is strengthened, the VBM of MoSe$_2$ gradually approaches the Fermi level (the Fermi level drops). At -0.4 V/Å, the PC$_6$/MoSe$_2$ heterostructure can also complete the transformation from type-I to type-II. The external electric field is considered to be a key strategy for modulating the electronic properties of PC$_6$/MoSe$_2$ heterostructures;

thus, PC$_6$/MoSe$_2$ will be widely applied in nano-electronic devices.

Figure 9 reveals the response of the average charge density difference of the PC$_6$/MoSe$_2$ heterojunction with the variation of external electric field. It can be seen that the fluctuation of charge density difference along Z-axis also raises as the intensity of the electric field enhances, which can facilitate the movement of band edges and signify a more forceful interplay at the bilayer interface. However, the total value of transferred charge cannot be read directly, so the number and direction of the total charge transferred are estimated by Bader analysis and listed in Table 2. The electrons transferred from PC$_6$ to MoSe$_2$ increase with the intensity of the positive electric field (0.0173|e| ~ 0.0658|e|). It is worth noting that in a small negative electric field, the direction of charge transfer is the same as that of under positive electric field, but the electrons transferred from PC$_6$ to MoSe$_2$ start to decrease, which is due to the reduced net effective internal electric field crossing the interface. After that, the PC$_6$ layer begins to receive electrons, which indicates that the size of the built-in electric field should be between 0.2 and 0.3 V/Å when the external electric field is zero. The applied electric field
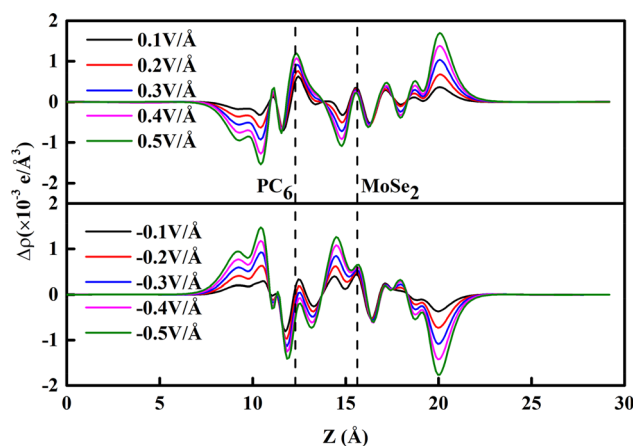

Figure 9 Averaged charge density difference of the PC$_6$/MoSe$_2$ heterojunction along the Z direction under various electric field. The black vertical dash lines indicate the position of PC$_6$ and MoSe$_2$ layer in the heterojunction.

Table 2 Charge transfer of $PC_6/MoSe_2$ heterostructure under the different vertical electric field (positive value means losing electrons, negative value means gaining electrons)

E_{ext}	0	0.1 V/Å	0.2 V/Å	0.3 V/Å	0.4 V/Å	0.5 V/Å
PC_6	0.0173|e|	0.0262|e|	0.0341|e|	0.0437|e|	0.0553|e|	0.0658|e|
E_{ext}	0	−0.1 V/Å	−0.2 V/Å	−0.3 V/Å	−0.4 V/Å	−0.5 V/Å
PC_6	0.0173|e|	0.0109|e|	0.0025|e|	−0.0049|e|	−0.0140|e|	−0.0215|e|

can change the distribution of charge and the accumulation of carriers, which in turn helps us grasp the charge transfer mechanism. This is due to the interaction between the built-in electric field and the external electric field.

The optical properties of $PC_6/MoSe_2$ heterostructure

The optical absorption of the $PC_6/MoSe_2$ heterojunction has been studied since the optical properties of materials play an important role in application of optoelectronic devices. The optical absorption coefficient can be calculated as follows [50]:

$$\alpha(\omega) = \sqrt{2}\omega[\sqrt{\varepsilon_1^2(\omega) + \varepsilon_2^2(\omega)} - \varepsilon_1(\omega)]^{1/2} \quad (5)$$

where $\varepsilon_1(\omega)$ and $\varepsilon_2(\omega)$ are the real and imaginary parts of the dielectric function. The imaginary part of the dielectric function is calculated as follows [50]:

$$\varepsilon_2(\omega) = \frac{4\pi^2 e^2}{V m^2 \varpi^2} \sum_{nn'\sigma} kn\sigma|p_i|kn'\sigma kn'\sigma|p_j|kn\sigma$$
$$\times f_{kn}(1 - f_{kn'})\delta(E_{kn'} - E_{kn} - \hbar\omega) \quad (6)$$

The optical absorption spectra of isolated PC_6 and $MoSe_2$ as well as the $PC_6/MoSe_2$ heterostructure are shown in Fig. 10a. It is clear that PC_6 has a wider absorption range than $MoSe_2$ in the infrared region, and the first absorption peak is also higher than $MoSe_2$, while $MoSe_2$ has a much larger absorption capacity in the visible and UV regions. Compared with that of the single layers, the absorption edge of the $PC_6/MoSe_2$ heterostructure has a redshift, which is more obvious compared with $MoSe_2$ and corresponds to the change of the band gap value. Evidently, the $PC_6/MoSe_2$ heterostructure combines the advantages of the two single layers. This phenomenon can be attributed to the overlap of electronic states, which is caused by the coupling between layers. According to the report of Peng et al. [51], the optical absorption of 10^5 cm^{-1} can be regarded as a sign of effective use of solar energy.

Therefore, the $PC_6/MoSe_2$ heterostructure has good utilization of solar energy.

Since the optical absorption spectra have the same changing trend under different biaxial strains and external electric fields, some representative results are shown in Fig. 9b, c. Successive redshifts and blueshifts can be observed with positive and negative biaxial strain, respectively, in Fig. 10b, which corresponds to the change in the band gap in Fig. 6a. As shown in Fig. 10c, it can be seen that the absorption of the heterojunction under the applied electric field has only a slight difference between 0 and 4.3 eV compared with 0 V/Å, while the heterostructure exhibits stronger UV absorption in the energy range of 4.3 to 6 eV. This is due to a new optical transition caused by electric field-induced charge transfer and interlayer coupling in the heterostructure.

Conclusion

In the work, the electronic properties of $PC_6/MoSe_2$ heterostructure under biaxial strain and external electric field are studied. It is also noticed that PC_6 is more sensitive to large compressive strains, while $MoSe_2$ is more sensitive to external electric fields. By applying biaxial strain, the band gap of the heterostructure can be adjusted approximately linearly within -5% to 5%. It can be found that the negative biaxial strain can make the $PC_6/MoSe_2$ heterostructure complete the transition from type-I to type-II, and the transition from semiconductor to metal can be achieved directly at 6%. In addition, the electric field can also significantly change the band structure of the $PC_6/MoSe_2$ heterojunction, which causes the heterojunction to undergo a transition from type-I to type-II under strong electric field. The charge transferred from PC_6 to $MoSe_2$ increases almost linearly by applying positive electric field, while if an electric field of −0.3 V/Å is applied, the direction of charge transfer changes, so the electric field can effectively adjust the charge distribution and
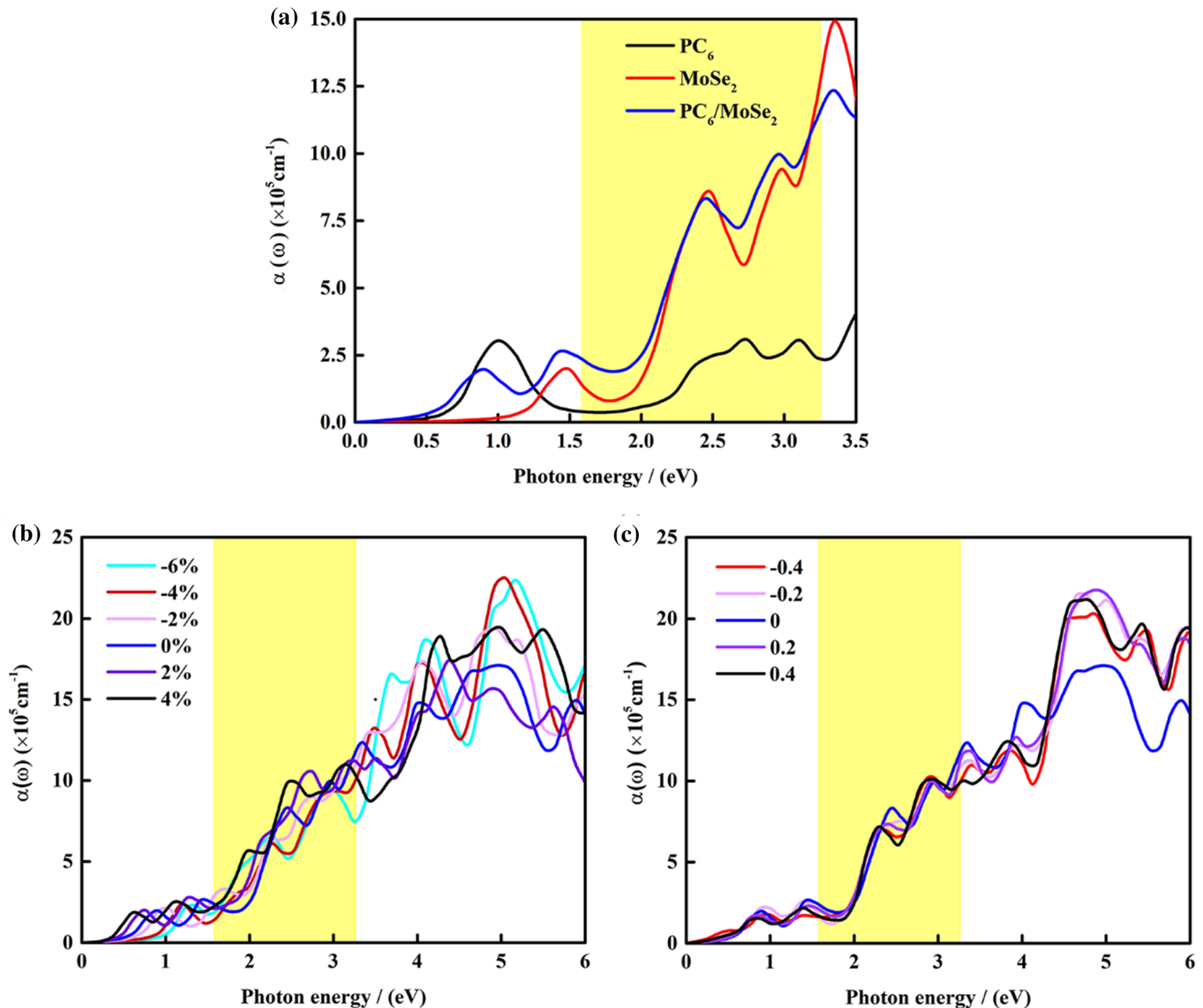
Figure 10 **a** Absorption coefficient of $PC_6/MoSe_2$ heterostructure, single-layer PC_6 and $MoSe_2$. The absorption spectra of $PC_6/MoSe_2$ heterostructure as a function of **b** biaxial strain and **c** electric field. The yellow area represents the visible light region.

carrier concentration. According to our results, the band alignment of the heterojunction can be adjusted under different electric fields and strains, so as to provide effective guidance for the follow-up research on the potential applications of $PC_6/MoSe_2$ heterostructure in multifunctional devices.

Declarations

Conflict of interest The authors declared that they have no conflicts of interest to this work.

References

[1] Lu WL, Nan HY, Hong JH, Chen YM, Zhu C, Liang Z, Ma XY, Ni ZH, Jin CH, Zhang Z (2014) Plasma-assisted fabrication of monolayer phosphorene and its Raman characterization. Nano Res 7:853–859

[2] Frank IW, Tanenbaum DM, van der Zande AM, McEuen PL (2007) Mechanical properties of suspended graphene sheets. J Vac Sci Technol B 25:2558–2561

[3] Rao F, Zhu G, Zhang WB, Gao JZ, Zhang FC, Huang Y, Hojamberdiev M (2021) In-situ generation of oxygen vacancies and metallic bismuth from $(BiO)_2CO_3$ via nitrogen assisted thermal-treatment for efficient and stable selective NO removal. Appl Catal B: Environmental 281:119481

[4] Lopez-Sanchez O, Lembke D, Kayci M, Radenovic A, Kis A (2013) Ultrasensitive photodetectors based on monolayer MoS_2. Nat Nanotechnol 8:497–501

[5] Yang S, Li Y, Wang X, Huo N, Xia JB, Li SS, Li J (2014) High performance few-layer GaS photodetector and its unique photo-response in different gas environments. Nanoscale 6:2582–2587

[6] Wei JL, Li W, Liao B, Bian BA (2020) Electronic and optical properties of vertical borophene/MoS_2 heterojunctions. Mater Chem Phys 252:123305

[7] Ru GL, Qi WH, Tang KW, Wei YR, Xue TW (2020) Interlayer friction and superlubricity in bilayer graphene and MoS_2/$MoSe_2$ van der Waals heterostructures. Tribol Int 151:106483

[8] Wang YZ, Huang R, Kong FJ, Gao BL, Li GN, Liang F, Hu G (2019) Tunable electronic and optical properties of the MoS_2/$MoSe_2$ heterostructure nanotubes. Superlattices Microstruct 132:106156

[9] Maji TK, Aswin JR, Mukherjee S, Alexander R, Mondal A, Das S, Sharma RK, Chakraborty NK, Dasgupta K, Sharma AMR, Hawaldar R, Pandey M, Naik A, Majumdar K, Pal SK, Adarsh KV, Ray SK, Karmakar D (2020) Combinatorial large-area MoS_2/Anatase$-TiO_2$ interface: a pathway to emergent optical and optoelectronic functionalities. ACS Appl Mater Interfaces 12(39):44345–44359

[10] Maji TK, Vaibhav K, Pal SK, Majumdar K, Adarsh KV, Karmakar D (2019) Intricate modulation of interlayer coupling at the graphene oxide/MoSe2 interface: Application in time-dependent optics and device transport. Phys Rev B 99(11):115309

[11] Ye HS, Sheng HH, Bai DM, Zhang JT, Wang JL (2020) Strain and electric field tuned electronic properties of BAs/$MoSe_2$ van der Waals heterostructures for alternative electrodes and photovoltaic cell in photocatalysis. Physica E 120:114055

[12] Gao W, Zhang F, Zheng ZQ, Li JB (2019) Unique and tunable photo-detecting performance for two-dimensional layered $MoSe_2$/WSe_2 P-N junction on 4H-SiC substrate. Appl Mater Inter 11:19277–19285

[13] Alkesh BP, Hiren KM, Payal C, Som N, Vijay D, Saurabh SS, Prafulla KJ, Gunvant KS, Kireetkumar DP, Vivek MP (2019) Electrophoretically deposited $MoSe_2$/WSe_2 heterostructure from ultrasonically exfoliated nanocrystals for enhanced electrochemical photoresponse. Appl Mater Inter 11:4093–4102

[14] Shin GH, Park C, Lee KJ, Jin HJ, Choi SY (2020) Ultrasensitive phototransistor based on WSe_2-MoS_2 van der waals heterostructure. Nano Lett 20:5741–5748

[15] Si K, Ma JY, Lu CH, Zhou YX, He C, Yang D, Wang XM, Xu XL (2020) A two-dimensional MoS_2/WSe_2 van der Waals heterostructure for enhanced photoelectric performance. Appl Surf Sci 507:145082

[16] Lu XH, Cui MX, Pan XC, Wang PF, Sun LJ (2020) Investigation of the structural and electronic properties of pristine and Au-embedded MoS_2/C60 and WSe_2/C60 van der Waals heterostructures: a first-principles study. Appl Surf Sci. 503:144328

[17] Zhong MZ, Zhang S, Huang L, You JB, Wei ZM, Liu XF, Li JB (2017) Large-scale 2D PbI_2 monolayers: experimental realization and their indirect band-gap related properties. Nanoscale 9:3736–3741

[18] Geim AK, Grigorieva IV (2013) Van der Waals heterostructures. Nature 499:419–425

[19] Kang J, Tongay S, Zhou J, Li JB, Wu JQ (2013) Band offsets and heterostructures of twodimensional semiconductors. Appl Phys Lett. 102:012111

[20] Nie JL, Gao JZ, Shen Q, Zhang WB, Rao F, Hojamberdiev M, Zhu GQ (2020) Flower-like $Bi0/CeO_2$-δ plasmonic photocatalysts with enhanced visible-light-induced photocatalytic activity for NO removal. J Sci China Mater 63:2272–2280

[21] Sun M, Wei XM, Zhang JM, Huang YH, Zhu GQ (2020) First-principles study on the type-II g-C_6N_6/GaS heterojunction: a promising photocatalyst for water splitting. Diamond Relat Mater. 110:108157

[22] You Y, Wei ML, Yang LK, Wang JW, Zhang YX, Xu J (2020) Multifunctional $MoSe_2$@rGO coating on the cathode versus the separator as an efficient polysulfide barrier for high-performance lithium-sulfur battery. Appl Surf Sci. 527:146785

[23] Tian PH, Tang T, Zhang J, Lin SJ, Huang GZ, Zeng JH, Kong Z, Wang HB, Xi JH, Ji ZG (2020) High photocatalytic and photoelectrochemical performance of a novel 0D/2D heterostructure photocatalyst constructed by ZnSe nanoparticles and $MoSe_2$ nanoflowers. Ceram Int 46:13651–13659

[24] Zhou SN, Wang MH, Wang JH, Xin HL, Liu SY, Wang ZJ, Wei SX, Lu XQ (2020) Carbon phosphides: promising electric field controllable nanoporous materials for CO_2 capture and separation. J Mater Chem A 8:9970–9980

[25] Yu T, Zhao ZY, Sun YH, Bergara A, Lin JY, Zhang ST, Xu HY, Zhang LJ, Yang GC, Liu YC (2019) Two-Dimensional PC_6 with Direct Band Gap and Anisotropic Carrier Mobility. J Am Chem Soc 141:1599–1605

[26] Zhang JN, Xu LQ, Yang C, Zhang XY, Ma L, Zhang M, Lu J (2020) Two-dimensional single-layer PC_6 as promising

anode materials for Li-ion batteries: The first-principles calculations study. Appl Surf Sci 510:145493

[27] Yu XF, Xiao L, Li YC (2020) PC_6 monolayer: A potential candidate as NOx sensor with high sensitivity and selectivity. Physica E 118:113958

[28] Li XP, Jia GR, Du J, Song XH, Xia CX, Wei ZM, Li JB (2018) Type-II $InSe/MoSe_2$ (WSe_2) van der Waals heterostructures: vertical strain and electric field effects. J Mater Chem C 6:10010–10019

[29] Ye JX, Liu JW, An YK (2020) Electric field and strain effects on the electronic and optical properties of $g\text{-}C_3N_4/WSe_2$ van der Waals heterostructure. Appl Surf Sci 501:144262

[30] Bai KF, Cui Z, Li EL, Ding YC, Zheng JS, Li C, Zheng YP (2020) YP Zheng, Electronic and optical characteristics of $GaS/g\text{-}C_3N_4$ van der Waals heterostructures: Effects of biaxial strain and vertical electric field. Vacuum 180:109562

[31] Li C, Xu Y, Sheng W, Yin WJ, Nie GZ, Ao Z (2020) A promising blue phosphorene/C_2N van der Waals type-II heterostructure as a solar photocatalyst: a first-principles study. Phys Chem Chem phys 22:615–623

[32] Khan MA, Erementchouk M, Hendrickson J, Leuenberger MN (2017) Electronic and optical properties of vacancy defects in single-layer transition metal dichalcogenides. Phys Rev B 95:245435

[33] Mahjouri-Samani M, Liang LB, Oyedele A, Kim YS, Tian MK, Cross N, Wang K, Lin MW, Boulesbaa A, Rouleau CM, Puretzky AA, Xiao K, Yoon M, Eres G, Duscher G, Sumpter BG, Geohegan DB (2016) Tailoring vacancies far beyond intrinsic levels changes the carrier type and optical response in monolayer $MoSe_{2-x}$ crystals. Nano Lett 16:5213–5220

[34] Kresse G, Furthmüller J (1996) Efficient iterative schemes for ab initio total-energy calculations using a plane-wave basis set. Phys Rev B: Condens Matter 54:11169–11186

[35] Kresse G, Hafner J (1994) Ab initio molecular-dynamics simulation of the liquid-metal-amorphous-semiconductor transition in germanium. Phys Rev B: Condens Matter 49:14251–14269

[36] Kohn W, Sham LJ (1965) Self-consistent equations including exchange and correlation effects. Phys Rev 140:A1133–A1138

[37] Hohenberg P, Kohn W (1964) Inhomogeneous electron gas. Phys Rev 136:B864–B871

[38] Blöchl PE (1994) Projector augmented-wave method. Phys Rev B: Condens Matter 50:17953–17979

[39] Kresse G, Joubert D (1999) From ultrasoft pseudopotentials to the projector augmented-wave method. Phys Rev B: Condens Matter 59:1758–1775

[40] Ernzerhof M, Scuseria GE (1999) Assessment of the Perdew-Burke-Ernzerhof exchangecorrelation functional. J Chem Phys 110:5029–5036

[41] Perdew JP, Chevary JA, Vosko SH, Jackson KA, Pederson MR, Singh DJ, Fiolhais C (1992) Atoms, molecules, solids, and surfaces: Applications of the generalized gradient approximation for exchange and correlation. Phys Rev B: Condens Matter 46:6671–6687

[42] Heyd J, Scuseria GE, Ernzerhof M (2003) Hybrid functionals based on a screened Coulomb potential. J Chem Phys 118:8207–8215

[43] Neugebauer S (1992) Adsorbate-substrate and adsorbate-adsorbate interactions of Na and K adlayers on Al (111). Phys Rev B 46:16067–16080

[44] Feibelman Peter J (2001) Surface-diffusion mechanism versus electric field: Pt/Pt(100). Phys Rev B 64:125403

[45] Zhao YF, Wang W, Li C, Sun YZ, Xu HF, Tu J, Ning J, Xu YB, He L (2018) Enhanced photocatalytic activity of nonmetal doped monolayer $MoSe_2$ by hydrogen passivation: first-principles study. Appl Surf Sci 456:133–139

[46] Wang Y, Sun YY, Zhang S, Lu TM, Shi J (2016) Band gap engineering of a soft inorganic compound PbI_2 by incommensurate van der Waals epitaxy. Appl Phys Lett 108:013105

[47] Shi H, Pan H, Zhang YW, Yakobson BI (2013) Quasiparticle band structures and optical properties of strained monolayer MoS_2 and WS_2. Phys Rev B: Condens Matter 87:155304

[48] Deng S, Li LJ, Li M (2018) Stability of direct band gap under mechanical strains for monolayer MoS_2, $MoSe_2$, WS_2 and WSe_2. Physica E 101:44–49

[49] Shu HB, Niu XH, Ding XJ, Wang Y (2019) Effects of strain and surface modification on stability, electronic and optical properties of GaN monolayer. Appl Surf Sci 479:475–481

[50] Vo DD, Idrees M, Pham VT, Vu TV, Nguyen ST, Phuc HV, Hieu NN, Binh Nguyen TT, Amin B, Nguyen CV (2020) Electronic structure and optical performance of $PbI_2/SnSe_2$ heterostructure. Chem Phys 533:110736

[51] Peng R, Ma YD, Huang BB, Dai Y (2019) Two-dimensional Janus PtSSe for photocatalytic water splitting under the visible or infrared light. J Mater Chem A 7:603–610